*Progress In Electromagnetics Research, Vol. 123, 427–445, 2012*

# A COMPREHENSIVE FACET MODEL FOR BISTATIC SAR IMAGERY OF DYNAMIC OCEAN SCENE

**Y.-W. Zhao[1], M. Zhang[1,*], X.-P. Geng[2], and P. Zhou[2]**

[1]School of Science, Xidian University, Xi'an 710071, China

[2]Science and Technology on Electromagnetic Scattering Laboratory, Beijing 100854, China

**Abstract**—A comprehensive facet model for bistatic synthetic aperture radar (Bis-SAR) imagery of dynamic ocean scene is presented in this paper. An efficient facet scattering model is developed to calculate the radar cross section (RCS) of the ocean surface for Bis-SAR firstly. Further more, this facet model is combined with a bistatic velocity bunching ($VB$) modulation of long ocean waves to obtain the Bis-SAR intensity expression in image plane of ocean scene. The displacement of the scatter elements in the image plane and the degradation of radar resolution in azimuth direction are quantificationally analyzed. Finally, Bis-SAR imagery simulations of ocean surface are illustrated, proving the validity and practicability of the presented algorithms.

## 1. INTRODUCTION

Synthetic aperture radar (SAR) has been successfully applied to the remote sensing of rough surface scene, in all weather, day and night. Over the ocean scene, it is influenced by varying surface winds, waves and currents, as well as the presence of surface material and oil spill. Many methodologies have been developed to depicture this field [1–7]. Due to technical limits, the maturely and extensively used SAR systems are the monostatic SAR (Mon-SAR) systems. However, Bis-SAR system can offer extra information of ocean scene compared with the Mon-SAR system for its unique geometry. In recent years, some key technologies in the Bis-SAR system such as the phase and time synchronization, location techniques are improved

*Received 9 October 2011, Accepted 26 December 2011, Scheduled 5 January 2012*

* Corresponding author: Min Zhang (mzhang@mail.xidian.edu.cn).

rapidly [8, 9]. Therefore, the application of Bis-SAR system and multistatic SAR (Mul-SAR) system on ocean scene has been more and more attention [10–16].

As we know, Bragg scattering plays a dominant role in backscattering for moderate wind speeds and incident angles away from nadir and grazing. Attempts have been made for decades to build an unified theory that can overwhelm most of the issues associated to the radar scattered estimation on ocean surface. The two-scale theory, under which the Bragg scattering contributions of the small ripples are tilted by the large scale components, has always been the most popular approach since it was introduced [17–23]. The essence of this approach is the theoretical division of the real surface with two types of irregularities: large waves whose radiuses of curvature are great enough for the evaluation by specular point theory, and fine ripples where the perturbation theory dominates. One composite-surface formula was accomplished by Valenzuela [19]. In this model, the ocean waves are assumed to be composed of an infinite number of slightly rough facets. And the net back-scattered power density is an average of the backscattered power from a single slightly rough facet over the distribution of slopes of the dominant ocean waves. This local fluctuation is an useful feature and desirable in ocean SAR imaging model as the mean SAR image may be represented simply as an appropriate superposition of the individual returns from separate surface facets [5, 24]. Alpers et al. discussed the Mon-SAR imaging mechanism based on this "facet-based" surface scattering models and the $VB$ modulations of ocean wave motions [25]. For his model in addition to the local incident modulation, the orbital motion of the water particles associated with the long ocean surface waves can also play an important role in the image formation, which leads to a nonuniform displacement of the scattering elements in the image plane, called $VB$ modulation. This is the imaging mechanism of ocean scene caused by varying velocities of the ocean wave elements. And a theoretical model is developed to relate ocean wave spectra to SAR image spectra of one dimensional monochromatic ocean waves [26]. His simulations reveal the basic features of the SAR imaging mechanism: If the nonlinearity of the imaging is sufficiently strong, the average velocity bunching parameter is suitable for characterizing the degree of nonlinearity. The amount of the azimuth shift of the spectral peak depends on the wave velocity, SAR integration time, and the width of ocean wave spectrum, etc.. Further more, a two-dimensional Monte-Carlo simulation has been applied in a comparison study of ocean wave spectra measured with a buoy and SAR image spectra obtained over the North Sea during the Shuttle Imaging Radar-

B (SIR-B) mission [27]. This model explores the most striking characteristic of SAR wave images for two-dimensional ocean waves: the pronounced asymmetries observed between the imaging of range and azimuthally traveling waves. However, there rarely any papers on the correct understanding of $VB$ modulation of this special and important mechanism for ocean SAR in bistatic case. So it is necessary to do some exploration in this field, which can provide a theoretical basis for applied research and system design of ocean Bis-SAR system.

This paper is to build an effective model for Bis-SAR imaging of two-dimensional ocean scene. Actually there are two primary steps to consider the Bis-SAR imagery mechanism of the dynamic ocean scene: First, to calculate the RCS of ocean scene for Bis-SAR; Second, to map the two-dimensional distribution of RCS into an image intensity distribution based on $VB$ model. For the first step, it is recognized that the wave-facet model is an effective model to calculate the backscattering radar cross section (RCS) of the ocean scene in general incidents [19]. However, it is not applicable to analyze the bistatic scattering properties of the facet modeling by means of the Bragg phenomena. And the $VB$ modulation on RCS must be taken into account to obtain the RCS of ocean scene for Bis-SAR. In our opinion, this model needs some improvement. So a more comprehensive facet model is proposed in this paper to describe the bistaitc scattering configurations of ocean scene. Further more, a $VB$ modulation function is induced to obtain the RCS of ocean for Bis-SAR. On the other hand, Bis-SAR data are often azimuth variant, because both the transmitter and the receiver have different motion trajectories and ocean waves move in range direction. So, for the second step, the Bis-SAR intensity expression in image plane of ocean is derived based on the geometry of Bis-SAR for ocean scene. It quantitatively describes the offset of target location in azimuth direction and the decline of the azimuth resolution. The Bis-SAR imagery of maritime scene is generated by an appropriate processing algorithm. Finally the perfect Bis-SAR simulation results are obtained, to prove the validity and practicability of the presented algorithm.

This paper begins by indicating how the two-dimensional Bis-SAR cross section distribution is mapped into an image intensity distribution based on $VB$ model in Section. 2. Section. 3 introduces the scattering mechanism of ocean surface for Bis-SAR. Section. 4 presents the concrete models and Bis-SAR imagery results.

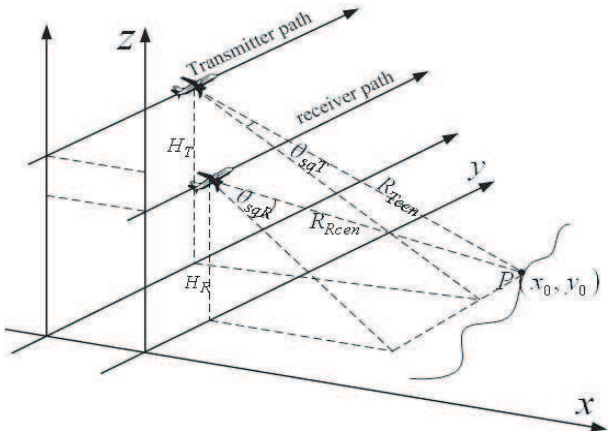


**Figure 1.** Bistatic SAR geometry with constant velocity of each platform.

## 2. MAPPING FUNCTION FROM RCS DISTRIBUTION TO IMAGE INTENSITY DISTRIBUTION FOR BIS-SAR

The Bis-SAR geometry is shown in Fig. 1. Let assume a moving target $P(x_0, y_0)$ at the ocean surface whose location relative to the transmitter and receiver is given by the distance $R_{Tcen}$ and $R_{Rcen}$ respectively at the beam center crossing time. Considering the motion of the target, the return signal is given as the follow.

$$sig(t, x_0, y_0) = \gamma(t, x_0, y_0) p\left(\tau - \frac{R(t, x_0, y_0)}{c}\right) \exp\left[-j\phi(t, x_0, y_0)\right] \quad (1)$$

where, $\tau$ is the range time and $t$ is the azimuth time, $p(\cdot)$ is the wide bandwidth encoded signal, $\gamma(t, x_0, y_0)$ is the complex bistatic scattering coefficient of target. $R$ is the instantaneous two-way range of the target.

$$\begin{aligned} R &= R_T(t) + R_R(t) + \Delta R \\ &= \sqrt{(Vt - y_0)^2 + R_{Tcen}^2 - 2(Vt - y_0) R_{Tcen} \sin\theta_{sqT}} \\ &\quad + \sqrt{(Vt - y_0)^2 + R_{Rcen}^2 - 2(Vt - y_0) R_{Rcen} \sin\theta_{sqR}} + \Delta R \end{aligned} \quad (2)$$

wherein, $R_T(t)$ and $R_R(t)$ are the instantaneous range of the stationary target to the transmitter and receiver. $\Delta R$ is the changes in range and azimuth of the target position due to the motion of ocean surface. The return signal phase $\phi(t, y_0, R)$ is proportional to $R$.

$$\phi(t, y_0, R) = k_e R = k_e \left[R_T(t) + R_R(t)\right] + \Delta\phi \quad (3)$$

where, $k_e$ is the wave number of incident wave, $\Delta\phi$ is the phase perturbation due to the target motions.

$$\begin{aligned}\Delta\phi &= -\int_0^t \vec{k}_t \cdot \left(\vec{u}\left(t'\right)+\vec{v}\right) dt' - \int_0^t \vec{k}_r \cdot \left(\vec{u}\left(t'\right)+\vec{v}\right) dt' \\ &= k_e \sum_{m=1}^{M}\sum_{n=1}^{N} \{[(\gamma_{by}\cos\varphi+\gamma_{bx}\sin\varphi)\sin(k_m x_0+k_n y_0-\omega_{mn}t+\varepsilon) \\ &\quad -\gamma_{in}\cos(k_m x_0+k_n y_0-\omega_{mn}t+\varepsilon)]\, a_{mn}(k_m,k_n) \\ &\quad -|\vec{v}|\, t(\gamma_{by}\cos\varphi_v+\gamma_{bx}\sin\varphi_v)\} \end{aligned} \tag{4}$$

where, $\gamma_{by} = \sin\theta_{sqT} + \sin\theta_{sqR} \cdot \gamma_{\text{in}} = \cos\theta_i + \cos\theta_s$, $\gamma_{bx} = \sqrt{\sin^2\theta_i - \sin\theta_{sqT}} + \sqrt{\sin^2\theta_s - \sin\theta_{sqR}}$, $\vec{k}_t$ and $\vec{k}_r$ are the wave vectors of transmitter and receiver. $\varphi$ is the angle between the flight direction and the direction of propagation of the long ocean wave. $\varphi_v$ is the angle between the flight direction and the surface current direction, $\vec{v}$ is the velocity of surface current, $a_{mn}\left(k_m,k_n\right)$ is proportional to the square root of gravity wave spectral density, $k_m$, $k_n$ are the component of sea spectrum along $x$ and $y$ directions, $\omega_{mn} = \sqrt{g(k_m^2+k_n^2)}$. $\vec{u}\left(\cdot\right)$ is the velocity of long ocean wave, whose vertical and horizontal velocity components can be expressed by the double superimposition model (DSM):

$$\begin{aligned} u_v(x_0,y_0,t) &= \sum_{m=1}^{M-1}\sum_{n=1}^{N-1} a_{mn}(k_m,k_n)(k_m,k_n)\cdot\omega_{mn} \\ &\quad \sin(k_m x_0+k_n y_0-\omega_{mn}t+\varepsilon) \\ u_h(x_0,y_0,t) &= \sum_{m=1}^{M-1}\sum_{n=1}^{N-1} a_{mn}(k_m,k_n)(k_m,k_n)\cdot\omega_{mn} \\ &\quad \cos(k_m x_0+k_n y_0-\omega_{mn}t+\varepsilon) \end{aligned} \tag{5}$$

The approximating function is taken as a second order polynomial of the form:

$$\bar{\Delta\phi} = \varphi_0 - k\left[\left(\bar{U}_T^r t+\frac{1}{2}A_T^r t^2\right)+\left(\bar{U}_R^r t+\frac{1}{2}A_R^r t^2\right)\right] \tag{6}$$

where, $\varphi_0$ is a constant, $\bar{U}_T^r$ and $A_R^r$ are the average speed and acceleration of the integration time respectively. Let $\int_{-T/2}^{T/2}\left(\Delta\phi-\bar{\Delta\phi}\right)^2 dt \to 0$,

one can obtain:

$$\bar{U}_T^r \approx \frac{1}{2}\sum_{m=1}^{M}\sum_{n=1}^{N}\omega\left\{\left[\left(\gamma_{by}\cos\varphi+\gamma_{bx}\sin\varphi\right)\cos(k_m x_0+k_n y_0+\varepsilon)\right.\right.$$
$$\left.+\gamma_{\text{in}}\sin(k_m x_0+k_n y_0+\varepsilon)\right]a_{mn}(k_m,k_n)+\frac{1}{2}\left|\vec{v}\right|\left(\gamma_{by}\cos\varphi_v\right.$$
$$\left.\left.+\gamma_{bx}\sin\varphi_v\right)\right\} \tag{7}$$

$$\bar{A}_T^r \approx \frac{1}{2}\sum_{m=1}^{M}\sum_{n=1}^{N}\omega^2 a_{mn}(k_m,k_n)\{[(\gamma_{by}\cos\varphi+\gamma_{bx}\sin\varphi)$$
$$\sin(k_m x_0+k_n y_0+\varepsilon)-\gamma_{\text{in}}\cos(k_m x_0+k_n y_0+\varepsilon)]\} \tag{8}$$

wherein, $T$ is the integration time. The amplitudes of transmitter and receiver antennas are weighted by the Gaussian function. Further more to simplify the calculation, the intensity changes with distance are not considered. The power density in the image plane can be obtained.

$$\left\langle\left|e\left(x,y,x_0,y_0\right)\right|^2\right\rangle$$
$$=\frac{\pi}{2}T^2\sigma\left(x_0,y_0\right)\frac{\rho_a}{\rho_a'}\exp\left[-\frac{\left(R_{Tcen}\sin\theta_{sqT}-R_{Tcen}\sin\theta_{sqT}\right)}{V^2T^2}\right]$$
$$\cdot\exp\left\{-\frac{\pi^2}{\rho_a'^2}\left[y-y_0+\frac{R_{Tcen}R_{Rcen}\left(\cos^2\theta_{sqT}\sin\theta_{sqT}+\cos^2\theta_{sqR}\sin\theta_{sqR}\right)}{R_{Tcen}\cos^2\theta_{sqT}+R_{Rcen}\cos^2\theta_{sqR}}\right.\right.$$
$$\left.\left.-\frac{2}{V}\frac{R_{Tcen}R_{Rcen}}{R_{Tcen}\cos^2\theta_{sqT}+R_{Rcen}\cos^2\theta_{sqR}}\bar{U}_T^r\right]^2\right\}f_r\left(x-x_0\right) \tag{9}$$

where, $\rho_{aN}=\lambda N_l/VT(\frac{\cos^2\theta_{sqT}}{R_{Tcen}}+\frac{\cos^2\theta_{sqR}}{R_{Rcen}})$, $\rho'_{aN}=\rho_{aN}\sqrt{1+\frac{\pi^2T^4\bar{A}_r^2}{\lambda^2}+\frac{T^2}{\tau_s^2}}$, $\tau_s$ the scene coherence time, $N_l$ is look number, $f_r\left(\cdot\right)$ the range resolution function, $\sigma\left(x_0,\,y_0\right)$ denotes the RCS of ocean for Bis-SAR. We know that the true positions of the scattering points and their positions in the image plane are not consistent from Eq. (9). If let

$$y' = y_0+\frac{2}{V}\frac{R_{Tcen}R_{Rcen}}{R_{Tcen}\cos^2\theta_{sqT}+R_{Rcen}\cos^2\theta_{sqR}}\bar{U}_T^r$$
$$-\frac{R_{Tcen}R_{Rcen}\left(\cos^2\theta_{sqT}\sin\theta_{sqT}+\cos^2\theta_{sqR}\sin\theta_{sqR}\right)}{R_{Tcen}\cos^2\theta_{sqT}+R_{Rcen}\cos^2\theta_{sqR}} \tag{10}$$

Then the power density in the image plane can be expressed by:

$$\left\langle \left| e\left(x,y,x_0,y'\right)\right|^2 \right\rangle = \frac{\pi}{2}T^2\frac{\rho_a}{\rho'_a}\frac{\sigma\left(x_0,y_0\right)}{\left|1+\frac{2}{V}\frac{R_{Tcen}R_{Rcen}}{R_{Tcen}\cos^2\theta_{sqT}+R_{Rcen}\cos^2\theta_{sqR}}\frac{\partial\tilde{U}_T^r}{\partial y_0}\right|}$$

$$\exp\left[-\frac{\left(R_{Tcen}\sin\theta_{sqT}-R_{Tcen}\sin\theta_{sqT}\right)}{V^2T^2}\right]\cdot\exp\left\{-\frac{\pi^2}{\rho'^2_a}\left[y-y'\right]^2\right\}f_r(x-x_0) \quad (11)$$

Because of the periodic non-uniform distribution of the velocity components in range direction, so the distribution of the scattering points in the image are together in some places and sparse in another places, resulting in the distribution of the intensity changes periodically in the image plane. Therefore, Bis-SAR image intensity distribution can be expressed as:

$$\begin{aligned}\langle I\left(x,y\right)\rangle &= \int_{-L_x/2}^{L_x/2}\int_{-L_y/2}^{-L_y/2}\left\langle\left|e\left(x,y,x_0,y'\right)\right|^2\right\rangle dx_0dy' \\ &= \frac{\pi}{2}T^2\exp\left[-\frac{\left(R_{Tcen}\sin\theta_{sqT}-R_{Tcen}\sin\theta_{sqT}\right)}{V^2T^2}\right]\int_{-L_x/2}^{L_x/2}\int_{-L_y/2}^{-L_y/2}\frac{\rho_a}{\rho'_a}f_r(x-x_0) \\ &\cdot\frac{\sigma(x_0,y_0)}{\left|1+\sum_{m=1}^{M}\sum_{n=1}^{N}g_{mn}a_{mn}(k_m,k_n)\cos(k_xx_0+k_yy_0+\varphi_v+\varepsilon)\right|}\cdot \\ &\exp\left\{-\frac{\pi^2}{\rho'^2_a}\left[y-y'\right]^2\right\} \end{aligned} \quad (12)$$

wherein

$$\begin{aligned} g_{mn} &= \frac{R_{Tcen}R_{Rcen}}{V\left(R_{Tcen}\cos^2\theta_{sqT}+R_{Rcen}\cos^2\theta_{sqR}\right)} \\ &\quad\cdot\omega k\cos\varphi\sqrt{\left(\gamma_{by}\cos\varphi+\gamma_{bx}\sin\varphi\right)^2+\gamma_{\text{in}}^2} \\ \varphi_v &= \tan^{-1}\left[\left(\gamma_{by}\cos\varphi+\gamma_{bx}\sin\varphi\right)/\gamma_{\text{in}}\right] \end{aligned} \quad (13)$$

## 3. SCATTERING MECHANISM OF OCEAN SURFACE FOR BIS-SAR

In this paper, we present comprehensive composite-surface facet model (CCSFM) and bistatic $VB$ modulation function to calculate the RCS of Bis-SAR. The Geometry of bistatic scattering for ocean surface is shown in Fig. 2, where, $\theta_i$ and $\phi_i$ is the depression and azimuth angle of incident wave respectively, $\theta_s$ and $\phi_s$ is the depression and azimuth angle of scattering wave respectively, $\hat{n}=(n_x,n_y,n_z)$ is the unit vector of the facet normal pointing to the air.

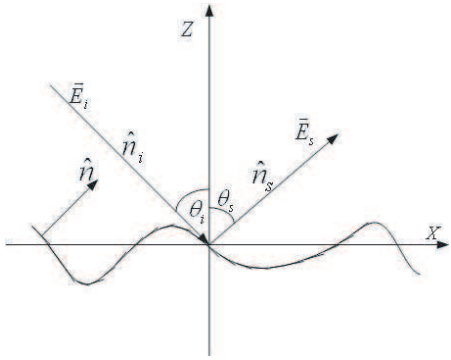


**Figure 2.** Geometry of bistatic scattering for ocean surface.

In terms of the surface elevation $z\,(x,\,y)$ associated with the large scale wave field, we have

$$\hat{n} = \left(-\frac{\partial z}{\partial x}, -\frac{\partial z}{\partial x}, 1\right)\left[1 + \left(\frac{\partial z}{\partial x}\right)^2 + \left(\frac{\partial z}{\partial x}\right)^2\right]^{-1} \tag{14}$$

$\hat{n}_i$ and $\hat{n}_s$ is the unit vector of incident and scattering waves respectively. Under far field approximation, the expression of $\hat{n}_i$ and $\hat{n}_s$ are described by

$$\begin{aligned} \hat{n}_i &= (\sin\theta_i \cos\phi_i, \sin\theta_i \sin\phi_i, -\cos\theta_i) \\ \hat{n}_s &= (\sin\theta_s \cos\phi_s, \sin\theta_s \sin\phi_s, \cos\theta_s) \end{aligned} \tag{15}$$

Let $\hat{v}_i$, $\hat{h}_i$ are the vertical and horizontal polarization unit vector of incident wave respectively, $\hat{v}_s$, $\hat{h}_s$ are the corresponding vertical and horizontal polarization unit vector of scattering wave respectively. They can be expressed as:

$$\begin{aligned} &\hat{h}_i{=}(-\sin\phi_i,\cos\phi_i)\ \ \hat{v}_i{=}\hat{h}_i{\times}\hat{n}_i{=}(-\cos\theta_i\cos\phi_i,-\cos\theta_i\sin\phi_i,-\sin\theta_i) \\ &\hat{h}_s{=}(-\sin\phi_s,\cos\phi_s)\ \ \hat{v}_s{=}\hat{h}_s{\times}\hat{n}_s{=}(\cos\theta_s\cos\phi_s,\cos\theta_s\sin\phi_s,-\sin\theta_s) \end{aligned} \tag{16}$$

When we calculate the oblique effect of large scale ocean waves, the local coordinate system is introduced which is defined as follows:

$$\begin{aligned} &\hat{z}'_i = \hat{n} \quad \hat{y}'_i = (\hat{n} \times \hat{n}_i)/|\hat{n} \times \hat{n}_i| \quad \hat{x}'_i = \hat{y}'_i \times \hat{z}'_i \\ &\hat{z}'_s = \hat{n} \quad \hat{y}'_s = (\hat{n} \times \hat{n}_s)/|\hat{n} \times \hat{n}_s| \quad \hat{x}'_s = \hat{y}'_s \times \hat{z}'_s \end{aligned} \tag{17}$$

Then the corresponding unit vectors of horizontal and vertical polarization are defined as:

$$\begin{aligned} &\hat{h}'_i = \hat{y}'_i \quad \hat{v}'_i = \hat{h}'_i \times \hat{n}_i \\ &\hat{h}'_s = \hat{y}'_s \quad \hat{v}'_s = \hat{h}'_s \times \hat{n}_s \end{aligned} \tag{18}$$

For horizontal/horizontal and vertical/vertical polarizations, the RCS in bistatic case per unit area by the bistatic two scale facet model (BTSFM):

$$\sigma_{hh} = 4\pi k_e^3 \cos^2\theta_{li} \cos^2\theta_{ls} \left| \left(\hat{h}_s \cdot \hat{h}'_s\right)^2 g_{vv}(\theta_{li}, \theta_{ls}, \phi_i, \phi_s) + \left(\hat{h}_s \cdot \hat{v}'_s\right)^2 g_{hh}(\theta_{li}, \theta_{ls}, \phi_i, \phi_s) \right|^2 \cdot E(k_{bx}, k_{by}) / [(\sin\theta_{li} + \sin\theta_{ls})/2] \quad (19)$$

$$\sigma_{vv} = 4\pi k_e^3 \cos^2\theta_{li} \cos^2\theta_{ls} \left| \left(\hat{v}_s \cdot \hat{h}'_s\right)^2 g_{vv}(\theta_{li}, \theta_{ls}, \phi_i, \phi_s) + \left(\hat{v}_s \cdot \hat{v}'_s\right)^2 g_{hh}(\theta_{li}, \theta_{ls}, \phi_i, \phi_s) \right|^2 \cdot E(k_{bx}, k_{by}) / [(\sin\theta_{li} + \sin\theta_{ls})/2] \quad (20)$$

where, $\theta_{li}$ and $\theta_{ls}$ is the local incident and scattering angle respectively, which can be obtained by $\cos\theta_{li} = \hat{n}_i \cdot n$, $\cos\theta_{ls} = \hat{n}_s \cdot n$. $g_{vv}(\theta_{li}, \theta_{ls}, \phi_i, \phi_s)$ and $g_{hh}(\theta_{li}, \theta_{ls}, \phi_i, \phi_s)$ are expressed as [28]:

$$g_{vv}(\theta_{li}, \theta_{ls}, \phi_i, \phi_s) = -\frac{(\varepsilon_r - 1)\cos\phi_s}{\left[\cos\theta_{li} + \sqrt{\left(\varepsilon_r - \sin^2\theta_{li}\right)}\right]\left[\cos\theta_{ls} + \sqrt{\left(\varepsilon_r - \sin^2\theta_{ls}\right)}\right]} \quad (21)$$

$$g_{hh}(\theta_{li}, \theta_{ls}, \phi_i, \phi_s) = (\varepsilon_r - 1) \cdot \frac{\left[\varepsilon_r \sin\theta_{li} \sin\theta_{ls} - \cos\phi_s \sqrt{\left(\varepsilon_r - \sin^2\theta_{li}\right)} \sqrt{\left(\varepsilon_r - \sin^2\theta_{ls}\right)}\right]}{\left[\varepsilon_r \cos\theta_{li} + \sqrt{\left(\varepsilon_r - \sin^2\theta_{li}\right)}\right]\left[\varepsilon_r \cos\theta_{ls} + \sqrt{\left(\varepsilon_r - \sin^2\theta_{ls}\right)}\right]} \quad (22)$$

$E(k_{bx}, k_{by})$ is the spectrum of the short Bragg scattering waves described by [29], $k_{bx}$, $k_{by}$ are the wave numbers

$$\begin{aligned} k_{bx} &= k\sin\theta_{ls}\cos\phi_s - k\sin\theta_{li}\cos\phi_i \\ k_{by} &= k\sin\theta_{ls}\sin\phi_s - k\sin\theta_{li}\sin\phi_i \end{aligned} \quad (23)$$

The bistatic RCS of real aperture radar can be calculated by Eqs. (19) and (20). However, when $k = \sqrt{k_{bx}^2 + k_{by}^2} \to 0$, this model is not applicable. Then, it has clear physical grounds to revise the BTSFM by a combination of Kirchhoff Approximation (KA) with BTSFM contributions, which is named CCSFM. In order to apply the facet two-scale Bragg theory, the facet must be large in comparison with the wavelength of the incident radiation in the facet plane, and be sufficiently small as it can still be regarded as a plane. We postulate the discrete facets in proper size, so that CCSFM can be used in the local summation frame for the bistatic RCS of real aperture radar.

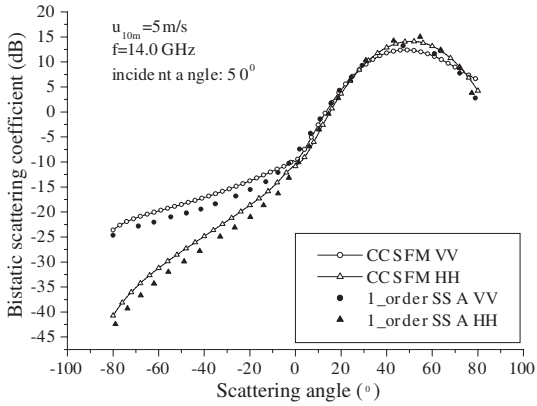


**Figure 3.** Comparison on bistatic RCS between SSA and CCSFM.

Figure 3 compares the results yielded by the first order SSA [30] with CCSFM for 5 m/s in $HH$ and $VV$ polarizations respectively, while the transmitter incident angle is 50°. It shows good agreement between 1-order SSA and CCSFM, as the difference remains within about 3 dB.

As shown in Fig. 1, the flight paths of transmitter and receiver are parallel to the $y$-axis direction with the same velocity $V$. Then, under this geometry, $k_{bx}$, $k_{by}$ is expressed as

$$\begin{aligned} k_{bx} &= k_e \left( \sqrt{\sin^2\theta_{li} - \sin^2\theta_{sqT}} + \sqrt{\sin^2\theta_{ls} - \sin^2\theta_{sqR}} \right) \\ k_{by} &= k_e \left( \sin\theta_{sqT} + \sin\theta_{sqR} \right) \end{aligned} \tag{24}$$

Figure 4 shows the distribution of RCS by the CCSFM for 5 m/s in $HH$ and $VV$ polarizations respectively. The transmitter depression angle is $\theta_i = 60°$, the receiver depression angle is $\theta_s = 50°$, the squint angle is $\theta_{sqT} = \theta_{sqR} = 30°$, the incident frequency is 14 GHz, the ocean surface is 500 m × 500 m. $\varphi = 90°$, it is the angle between the flight direction and the direction of propagation of the long ocean wave. It is shown in the figures that the intensity of $VV$ polarization is large than that of $HH$ polarization and the corresponding distribution of intensity is inconsistent with that of ocean surface slope.

As we know, SAR image of ocean scene is generated after the modulation of small-scale waves in space and time are indirectly obtained by SAR system. Spatial modulation is the stationary wave imaging mechanism of real aperture radar. Modulation in time is the effect of ocean wave movement to the SAR imaging, mainly $VB$ modulation. Here we discuss the $VB$ modulation on the RCS of Bis-SAR. The function of $VB$ modulation can be expressed as the follow based on the geometry of Bis-SAR.

$$T_k^{VB} = g_{mn} \cdot \exp\left(j\varphi_v\right) \tag{25}$$

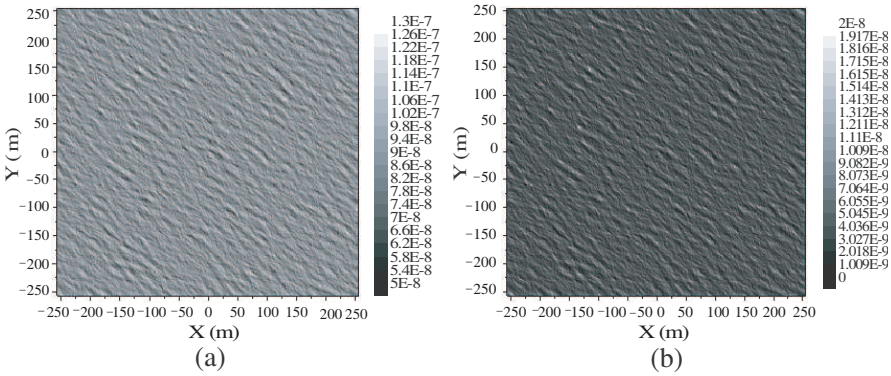


**Figure 4.** Distribution of RCS calculated by CCSFM. (a) $VV$ polarization (b) $HH$ polarization.

Then the RCS of ocean surface for Bis-SAR model is calculated by linear modulation function [31].

$$\sigma_{\text{sea}}(x_0, y_0, t) = \sigma_{\text{DSBFM}} |1 + f(x_0, y_0, t)|^{-1} \tag{26}$$

where

$$f(x_0, y_0, t) = \sum_{m=1}^{M-1} \sum_{n=1}^{N-1} a_{mn} b_{mn} g_{mn} \cdot \cos(k_m y_0 + k_n x_0 - \omega_{mn} t + \varepsilon + \phi_v) \tag{27}$$

wherein,

$$b_{mn} = \sin c\left(\frac{k_m \Delta y}{2}\right) \cdot \sin c\left(\frac{k_n \Delta x}{2}\right) \cdot \sin c\left(\frac{\omega_{mn} T}{2}\right) \tag{28}$$

Figure 5 shows the distribution of RCS for Bis-SAR simulated by the CCSFM and $VB$ modulation for 5 m/s in $HH$ and $VV$ polarizations respectively. The corresponding parameters are the same as Fig. 4. It can be seen from the figure, the offsets of scattering points in the azimuth direction are non-uniform, because the velocity components in incident direction and scattering direction are non-uniform distribution along azimuth direction.

## 4. SIMULATION RESULTS

In order to verify the performance of the proposed method, Bis-SAR imaging simulation results on the ocean scene are taken for example. The simulation parameters of Bis-SAR are shown in Table 1. And, in generating realizations of the Bis-SAR imaging simulations for the surface wave field, the JONSWAP form is used for growing

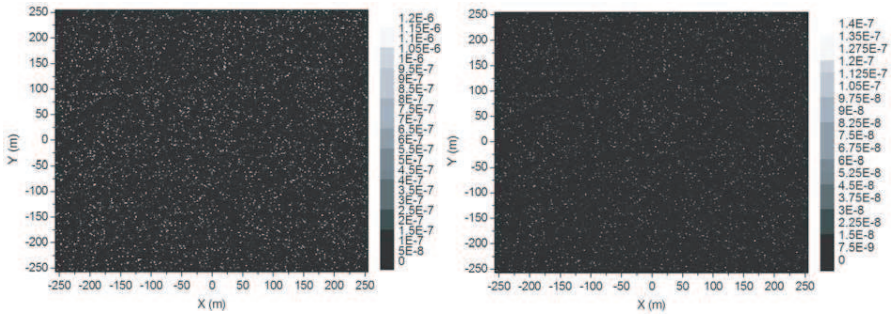


**Figure 5.** Distribution of RCS calculated by CCSFM and $VB$ modulation. (a) $VV$ polarization (b) $HH$ polarization.

**Table 1.** Simulation parameters of Bis-SAR.

| Para. / SAR | $\lambda(m)$ | $\theta_T$ | $\theta_R$ | $\theta_{sqT}$ | $\theta_{sqR}$ | $\left(\frac{R}{V}\right)_T$ | $\left(\frac{R}{V}\right)_R$ | $T\,(s)$ | $N_l$ |
|---|---|---|---|---|---|---|---|---|---|
| SPA-SAR | 0.23 | $5\pi/36$ | $\pi/6$ | $-\pi/9$ | $\pi/9$ | 120 | 100 | 2.25 | 4 |
| AIR-SAR | 0.03 | $\pi/4$ | $\pi/3$ | $-\pi/8$ | $\pi/8$ | 60 | 40 | 0.2 | 2 |

**Table 2.** Ocean parameters used in the simulation.

| Sea state | $\alpha$ | $\gamma$ | $\phi_m\,(^\circ)$ | $U\,(\mathrm{ms}^{-1})$ |
|---|---|---|---|---|
| Growing windsea I | 0.01 | 3.3 | 0° | 10 |
| Growing windsea II | 0.01 | 3.3 | 30° | 10 |
| Developed I | 0.0081 | 1 | 30° | 10 |
| Developed II | 0.0081 | 1 | 0° | 10 |

windsea spectra and fully developed spectra with appropriate choice of parameters respectively shown as Table 2 [31].

The growing windsea surfaces with $500 \times 500\,\mathrm{m}^2$ are shown in Fig. 6, in which the parameters are set as Growing windsea I and Growing windsea II for (a) and (b) respectively.

The corresponding AIR-SAR (Airborne-SAR) imageries of the ocean surface at $VV$ polarization are shown in Figs. 7(a) and (b). And, the corresponding SPA-SAR (Spaceborne-SAR) imageries of ocean surface at $VV$ polarization are shown in Figs. 8(a) and (b). The brightness in the imageries shows the scattering intensity per resolution cell, where the intensity is proportional to the surface height. It is shown that the azimuth resolution is degraded with the reduction of

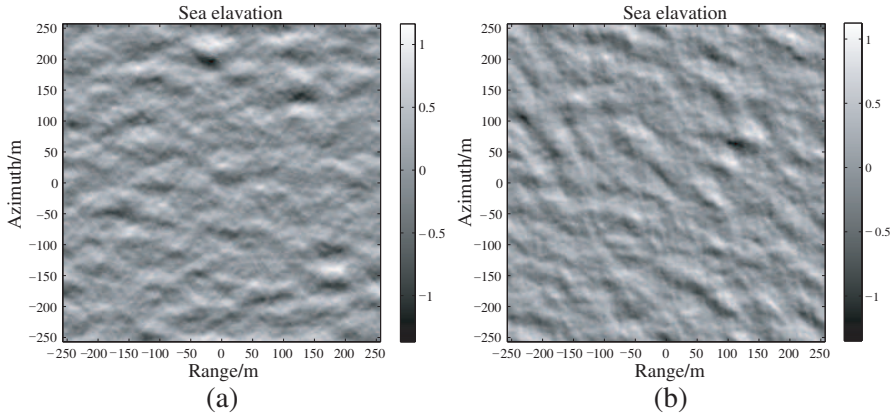


**Figure 6.** Two dimensional sea elevation. (a) Growing windsea I. (b) Growing windsea II.

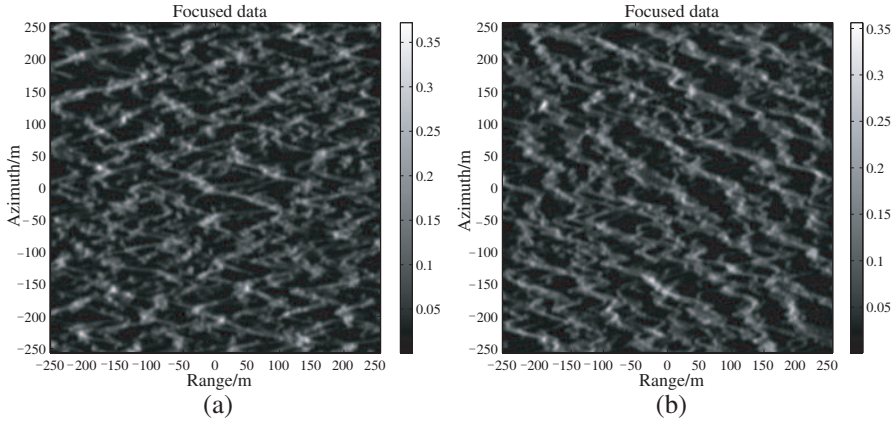


**Figure 7.** Bis-SAR imagery of the ocean surface (AIR-SAR). (a) Growing windsea I, $VV$ polarization. (b) Growing windsea II, $VV$ polarization.

$\phi_m$ for the same wind speed. However it is not so visible as the Mon-SAR. The change of $R/V$ and $\lambda$ and the related time of sea surface also affect the resolution of Bis-SAR. The image intensity of SPA-SAR is much greater than that of AIR-SAR. This is due to the incidence angle and scattering angle of SPA-SAR are relatively small, so the scattering coefficient is greater than that of AIR-SAR. In addition, the synthetic aperture of SPA-SAR is longer than that of AIR-SAR and the attenuation of electromagnetic field with distance is not considered in the simulation.

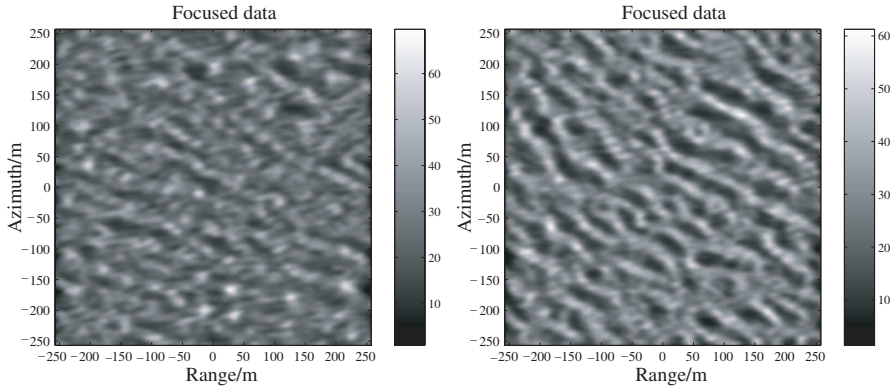


**Figure 8.** Bis-SAR imagery of the ocean surface (SPA-SAR). (a) Growing windsea I, $VV$ polarization. (b) Growing windsea II, $VV$ polarization.

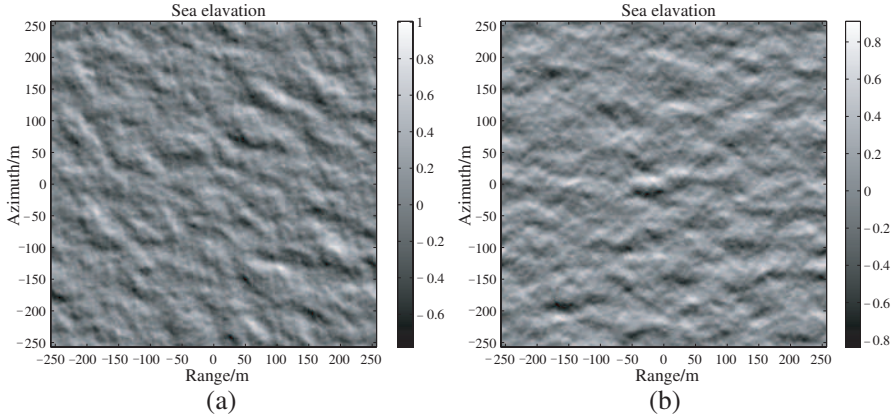


**Figure 9.** Two dimensional sea elevation. (a) Developed I. (b) Developed II.

The modulation of velocity bunching is sensitive to the direction of sea wave propagation. Position migration and image blur are more serious with the increase of wind velocity. The developed sea surfaces with $500 \times 500\,\mathrm{m}^2$ are shown in Fig. 9, in which the parameters are set as Developed I and Developed II for (a) and (b) respectively.

The corresponding AIR-SAR imageries of the ocean surface at $VV$ polarization are shown in Figs. 10(a) and (b). And, the corresponding SPA-SAR imageries of ocean surface at $VV$ and $HH$ polarization are shown in Figs. 11(a) and (b) respectively. The figures show that the intensities at $HH$ polarization are smaller than that of $VV$

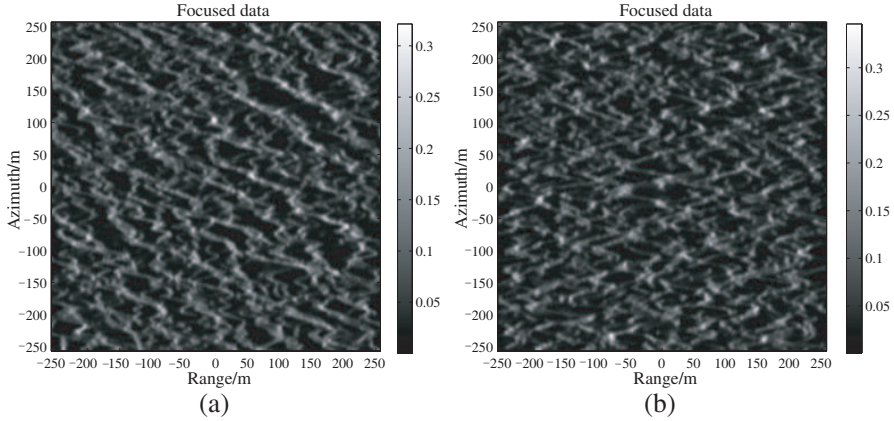


**Figure 10.** Bis-SAR imagery of the ocean surface (AIR-SAR). (a) Developed I ($VV$ polarization). (b) Developed II ($VV$ polarization).

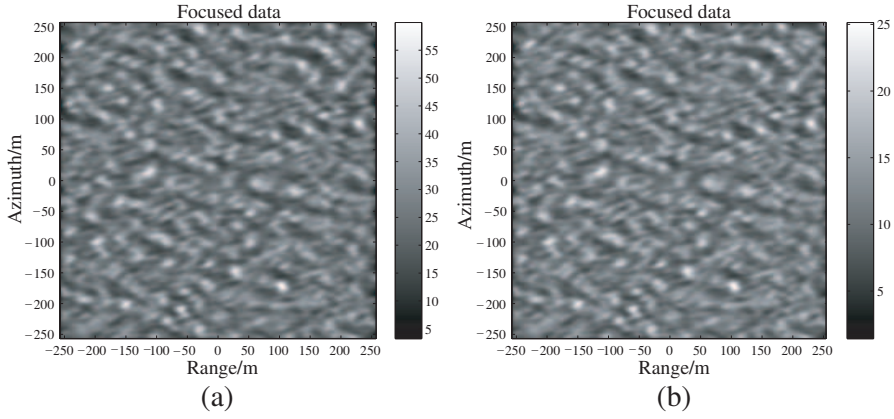


**Figure 11.** Bis-SAR imagery of the ocean surface (SPA-SAR). (a) $VV$ polarization. (b) $HH$ polarization.

polarization. And SAR imaging of ocean waves at $VV$ polarization is better than that of $HH$ polarization. This is because $VV$ polarization has dominant mean Bistatic RCS of ocean scene over $HH$ polarization and $VV$ polarization has the same $VB$ modulation as $HH$ polarization under the same sea state and Simulation parameters of Bis-SAR. At the same wind condition, the intensity of SAR image for growing windsea is greater than that of developed sea surface. This is because, at the same wind speed, the fluctuations of growing windsea are slightly

larger than that of developed sea surface and the overall fluctuations of developed sea surface are more uniform, which are in line with the natural laws of wind sea waves. These results are in accordance with that of observations [32, 33]. So it provides a theoretical basis for the application of Bis-SAR system in the marine scene.

## 5. CONCLUSIONS

In order to meet the development of Bis-SAR on ocean scene, the present paper extends current models on the imaging mechanism of ocean waves by monostatic SAR (Mon-SAR). Theoretical models for describing the imaging mechanism of ocean waves by Bis-SAR for low to moderate sea states are discussed in this paper. We investigate the bistatic scattering mechanism of the ocean surface by applying the CCSFM, when ocean surface waves are detected by Bis-SAR. In addition, $VB$ modulation and degradation in resolution due to wave motions in the imaging process by Bis-SAR are investigated furthermore. The perfect Bis-SAR simulation results of ocean surface are obtained. This proposed algorithm modifies the available models of electromagnetic scattering and bistatic SAR imagery from large ocean scene, which provide a foundation for applied research and system design.

## ACKNOWLEDGMENT

The authors would like to thank the anonymous reviewers for their invaluable comments and suggestions, which lead to great improvement of our manuscript, and also thank the National Natural Science Foundation of China under Grant No. 60871070, the Fundamental Research Funds for the Central Universities and the Foundation of the National Electromagnetic Scattering Laboratory to support this kind of research.

## REFERENCES

1. Zecchetto, S., F. De Biasio, and P. Trivero, "A wavelet technique to extract the backscatter signatures from SAR images of the sea," *PIERS Online*, Vol. 5, No. 7, 696–700, 2009.
2. Hasselmann, K., R. K. Raney, W. Alpers, R. A. Shuchman, D. R. Lyzenga, C. L. Rufenach, and M. J. Tucker, "Theory of synthetic aperture radar ocean imaging: A MARSEN view," *Journal of Geophysical Research*, Vol. 90, 4659–4686, 1985.

3. Chan, Y. K. and V. C. Koo, "An introduction to synthetic aperture radar (SAR)," *Progress In Electromagnetics Research B*, Vol. 2, 27–60, 2008.
4. Zhao, Y. W., M. Zhang, and H. Chen, "An efficient ocean SAR raw signal simulation by employing fast fourier transform," *Journal of Electromagnetic Waves and Applications*, Vol. 24, No. 16, 2273–2284, 2010.
5. Franceschetti, G., "On ocean SAR raw signal simulation," *IEEE Trans. on Geosci. and Remote Sensing*, Vol. 36, 84–100, 1998.
6. Zhang, M., Y. W. Zhao, H. Chen, and W.-Q. Jiang, "SAR imaging simulation for composite model of ship on dynamic ocean scene," *Progress In Electromagnetics Research*, Vol. 113, 395–412, 2011.
7. Baussard, A., M. Rochdi, and A. Khenchaf, "PO/mec-based scattering model for complex objects on a sea surface," *Progress In Electromagnetics Research*, Vol. 111, 229–251, 2011.
8. Wu, J., J. Yang, Y. Huang, Z. Liu, and H. Yang, "A new look at the point target reference spectrum for bistatic SAR," *Progress In Electromagnetics Research*, Vol. 119, 363–379, 2011.
9. Sun, J., S. Mao, G. Wang, and W. Hong, "Polar format algorithm for spotlight bistatic SAR with arbitrary geometry configuration," *Progress In Electromagnetics Research*, Vol. 103, 323–338, 2010.
10. Gierull, C. H., "Bistatic synthetic aperture radar," Technical Report, DRDC Ottawa, TR 2004-190, November 2004.
11. Loffeld, O., H. Nies, V. Peters, and S. Knedlik, "Models and useful relations for bistatic SAR processing," *IEEE Trans. on Geosci. and Remote Sensing*, Vol. 42, 2031–2038, 2004.
12. Yarman, C. E., B. Yazici, and M. Cheney, "Bistatic synthetic aperture radar imaging for arbitrary flight trajectories," *IEEE Transactions on Image Processing*, Vol. 17, 84–93, 2008
13. Comblet, F., A. Khenchaf, A. Baussard, and F. Pellen, "Bistatic synthetic aperture radar imaging: Theory, simulations and validations," *IEEE Trans. on Antennas and Propagat.*, 3529–3540, Vol. 54, No. 11, November 2006.
14. Arnold-Bos, A., A. Khenchaf, and A. Martin, "Bistatic radar imaging of the marine environment Part I: Theoretical background," *IEEE Trans. on Geosci. and Remote Sensing*, 3372–3383, Vol. 45 No. 1, November 2007.
15. Arnold-Bos, A., A. Khenchaf, and A. Martin, "Bistatic radar imaging of the marine environment. Part 2: Simulation and results analysis," *IEEE Trans. on Geosci. and Remote Sensing*, 3384–3396, Vol. 45, No. 11, November 2007.

16. Kassem, M. J. B., J. Saillard, and A. Khenchaf, "BISAR mapping I. theory and modeling," *Progress In Electromagnetics Research*, Vol. 61, 39–65, 2006.
17. Bass, F.G. and I. M. Fuks, *Wave Scattering from Statistically Rough Surfaces*, 418–442, Pergamon Press Oxford, New York, 1979.
18. Ji, W.-J. and C.-M. Tong, "Bistatic scattering from two-dimensional dielectric ocean rough surface with a PEC object partially embedded by using the g-smcg method," *Progress In Electromagnetics Research*, Vol. 105, 119–139, 2010.
19. Valenzuela, G. R., "Theories for the interaction of electromagnetic and oceanic waves — A review," *Boundary-Layer Meteorology*, Vol. 13, 61–85, 1978.
20. Vaitilingom, L. and A. Khenchaf, "Radar cross sections of sea and ground clutter estimated by two scale model and small slope approximation in hf-VHF bands," *Progress In Electromagnetics Research B*, Vol. 29, 311–338, 2011.
21. Qi, C., Z. Zhao, W. Yang, Z.-P. Nie, and G. Chen, "Electromagnetic scattering and doppler analysis of three-dimensional breaking wave crests at low-grazing angles," *Progress In Electromagnetics Research*, Vol. 119, 239–252, 2011.
22. Taboada, J. M., M. G. Araujo, J. M. Bertolo, L. Landesa, F. Obelleiro, and J. L. Rodriguez, "MLFMA-FFT parallel algorithm for the solution of large-scale problems in electromagnetics," *Progress In Electromagnetics Research*, Vol. 105, 15–30, 2010.
23. Bass, F. G., I. M. Fuks, et al., "Very high frequency radiowave scattering by a disturbed sea surface," *IEEE Trans. on Antennas and Propagat.*, Vol. 16, No. 5, 554–568, 1968.
24. Franceschetti, G., M. Migliaccio, D. Riccio, and G. Schirinzi, "SARAS: A synthetic aperture radar (SAR) raw signal simulator," *IEEE Trans. on Geosci. and Remote Sensing*, Vol. 30, 110–123, 1992.
25. Alpers, W. R., D. B. Ross, and C. L. Rufenach, "On the detectability of ocean surface waves by real and synthetic aperture radar," *Journal of Geophysical Research*, Vol. 86, 6481–6498, 1981.
26. Alers, W., "Monte carlo simulations for studying thc relationship between ocean wave and synthetic aperture radar image spectra," *Journal of Geophysical Research*, Vol. 88, 1745–1759, 1983.
27. Alpers, W., C. Bruning, and K. Richter, "Comparison of simulated and measured synthetic aperture radar image spectra with buoy-derived ocean wave spectra during the shuttle imaging

radar-B mission," *IEEE Trans. on Geosci. and Remote Sensing*, Vol. 24, 559–566, 1986.

28. Ishimaru, A., *Wave Propagation and Scattering in Random Media*, Academic Press, New York, 1978.
29. Fung, A. K. and K. Lee, "A semi-empirical sea-spectrum model for scattering coefficient estimation," *IEEE J. Oceanic Engineering*, Vol. 7, No. 4, 166–176, 1982.
30. Awada, A, M. Y. Ayari, A. Khenchaf, and A. Coatanhay, "Bistatic scattering from an anisotropic sea surface: Numerical comparison between the first-order SSA and the TSM models," *Waves in Random and Complex Media*, Vol. 16, No. 3, 383–394, 2006.
31. Bruninng, C., W. Alpers, and K. Hasselmann, "Monte-carlo simulation studies of the nonlinear imaging of a two dimensional surface wave field by a SAR," *International Journal of Remote Sensing*, Vol. 11, 1695–1727, 1990.
32. Vachon, P. W., "Ship detection by RADARSAT SAR: Validation of detection model predictions," *Canadian Journal of Remote Sensing*, Vol. 23, 48–59, 1997.
33. Arnold-Bos, A., A. Khenchaf, and A. Martin, "Bistatic radar imaging of the marine environment, Part 2: Simulation and results analysis," *IEEE Trans. on Geosci. and Remote Sensing*, Vol. 45, No. 11, 3384–3396, 2007.